Deep Surface Trap Filling by Photoinduced Carriers and Interparticle Electron Transport Observed in TiO2 Nanocrystalline Film with Time-Resolved Visible and Mid-IR Transient Spectr...

ARTICLE *in* THE JOURNAL OF PHYSICAL CHEMISTRY C · FEBRUARY 2007

Impact Factor: 4.77 · DOI: 10.1021/jp0645566

3 AUTHORS, INCLUDING:

Yu-Xiang Weng
Chinese Academy of Sciences
45 PUBLICATIONS **780** CITATIONS

Deep Surface Trap Filling by Photoinduced Carriers and Interparticle Electron Transport Observed in TiO_2 Nanocrystalline Film with Time-Resolved Visible and Mid-IR Transient Spectroscopies

Hui Zhao, Qingli Zhang, and Yu-Xiang Weng*

Laboratory of Soft Matter Physics, Institute of Physics, Chinese Academy of Sciences, Beijing 100080, China, and National Laboratory of the Condensed Matter Physics, Beijing 100080, China

Received: July 19, 2006; In Final Form: September 20, 2006

TiO_2 nanocrystal and TiO_2-xSiO_2 core/shell films were investigated by band gap excitation followed by detection of the photoinduced carriers with time-resolved transient absorption spectroscopy in both the visible and mid-IR range. The passivation of the TiO_2 nanocrystal with the SiO_2 shell has two goals, that is, reducing the surface-trapped states and segregating the TiO_2 nanoparticles in the sintered film to prevent interparticle carrier migration. The results show that within the accessible mid-IR range (5−6.5 μm) the observed transient absorptions of the TiO_2 crystal and TiO_2-xSiO_2 core/shell films exhibit an IR spectrum typical of intraband transition of free electrons where the observed absorption intensity is proportional to λ^p (λ = wavelength/μm), and p was determined as 2.6 for the TiO_2 nanoparticle film and 4.9 for the TiO_2-xSiO_2 core/shell composite film, respectively. Three typical kinetic phases for the transient IR absorption decay profile of the TiO_2 film have been observed, that is, a rapid decay beyond the instrumental response time (∼80 ns), a bleaching recovery with a rising time constant around 1.8 μs, and a very slow absorption decay component. The rapid decay phase is assigned as the free carrier recombination within the bulk crystal, whereas the bleaching recovery corresponds to the filling of the deep trapping sites by the shallow trapped electrons, and finally the very slow absorption component is assigned to the interparticle electron transport and deep trapped electron−hole recombination. For the TiO_2-xSiO_2 core/shell film, only the rapid decay phase can be observed. During the visible light detection, a broad-band transient absorption with a peak located at about 650 nm has been observed for the TiO_2 nanoparticle film, which is expected for the absorption from the shallow trapped electrons, while the corresponding carrier relaxation kinetics can be fitted by a monoexponential decay with a time constant of about 1.8 μs, correlating well to the deep trap filling process revealed by IR absorption. It is thus assigned as the filling of the deep trapped sites by the shallow trapped electrons. In contrast, no observable transient absorption can be detected at 650 nm for the TiO_2-xSiO_2 core/shell film. As a result, the facts from both the IR and visible light detections indicate that the passivation of SiO_2 reduces the density of the trapped state on TiO_2 nanoparticle surface substantially and blocks the interparticle carrier migration efficiently.

1. Introduction

Wide band gap semiconductor TiO_2 has been used widely in many application fields, such as degradation of environmental pollutants,[1−6] solar energy conversion,[7,8] and so forth. Owing to its excellent photocatalytic properties, TiO_2 has attracted intensive research interest.[9,10] In general, either the photocatalytic or photon-to-electron conversion efficiency of TiO_2 is determined by the competition between the unavoidable carrier recombination and the intended charge-transfer reaction. It has been shown that the carrier recombination and inter- or intraparticle charge migration depends strongly on the surface trap states.[11−13] Therefore, the nature of electron trapping on the TiO_2 surface is of great importance to the above fields.

Trap states on the TiO_2 nanoparticle surface turn out to be a subject of extensive studies, yet not having been clearly understood. Several groups have reported that the trap states lie below the conduction-band edge of nanocrystalline TiO_2.[14−18] These states have been assigned to the Ti^{3+} state.[13] It is believed that the conduction band is composed of Ti 3d, 4s, and 4p orbitals; the Ti 3d orbitals dominate the lower portion of the conduction band.[18,19] It has been suggested that the electronic states due to the trapped electron (Ti^{3+}) are located in the band gap.[20] The high density of these states has been associated, at least in part, with the high surface area/volume ratio of TiO_2 crystalline films, and these trap states would affect the charge recombination kinetics inevitably. Durrant and co-workers have demonstrated that the charge recombination kinetics observed on the dye-sensitized TiO_2 film can be independent of the different sensitizers used and are dominated by the interparticle electron transport process.[11−13] A typical feature of charge recombination at the dye-sensitized TiO_2 nanocrystalline film is that it contains much slower nonexponential recombination kinetics, which extends to a millisecond or longer time scale and can be expressed by "stretched" exponential kinetics. For the interfacial charge recombination, the adsorbed dye cation is fixed at the nanoparticle surface, while the injected electron undergoes spatial migration[12] as well as energy relaxation where the electron relaxes from the conduction band to the trap states.[9] Energy relaxation was observed by the comparison between the

* To whom correspondence should be addressed: Phone: 86-10-82648118; fax: 86-10-82649451; e-mail: yxweng@aphy.iphy.ac.cn.

10.1021/jp0645566 CCC: $37.00
Published on Web 02/10/2007

charge recombination kinetics of the adsorbed oxidized dye cation with the injected electron and conduction-band electron decay kinetics by femtosecond time-resolved IR difference spectroscopy.[21] It is concluded that the charge recombination kinetics are mainly affected by electron trapping on the TiO_2 surface as well as electron transport within the film.[12,13] In addition to the photoinduced charge recombination, investigation of the photoinduced carrier-only relaxation process would be more informative because its corresponding kinetics are free of interference from the charge recombination between the trapped electron and the oxidized dye cation. Furthermore, Szczepankiewicz et al. [22] have investigated the free and trapped charge carrier relaxation kinetics; they concluded that the photogenerated free electrons are comparable to conduction-band electrons injected from surface-bound chromophores.

Time-resolved transient absorption spectroscopy from femtoseconds to milliseconds has been used extensively to study the relaxation and recombination processes of the photogenerated carriers within semiconductor samples.[14−18,22−26] Recently, a number of studies on the photoinduced carrier dynamics within TiO_2 nanocrystalline film by the use of transient absorption spectroscopy in visible and mid-IR ranges have been reported. Tachiya and co-workers[24] studied transient absorption spectroscopy in a spectral region from 400 to 2500 nm, and the absorption spectrum of the electron was obtained through a hole-scavenging reaction under steady-state light irradiation. They concluded that there are three reactive species on the nanoparticle TiO_2 film, that is, trapped holes and free and trapped electrons, where the trap sites are distributed mainly at the surface of particles and free electrons are located inside the bulk. A broad absorption spectrum in the detected region shows a $\lambda^{1.7}$ intensity/wavelength dependence that was assigned as the free electron absorption. Yamakata et al.[23,25] investigated the kinetics of photoinduced carriers within TiO_2 nanoparticles in reaction with oxygen and water molecules. They reported a similar broad absorption between 3000 and 1000 cm^{-1} showing a $\lambda^{1.5}$ absorption intensity/wavelength dependence, which is attributed to the shallow trapped electron absorption. Hoffmann and co-workers[22,26] also observed a transient broad-band absorption with a $\lambda^{1.7}$ intensity dependence that produced by band gap irradiation. Besides, they have also observed a broad IR absorption peak centered at 3380 cm^{-1}, which is free from the deuterium/hydrogen exchange effect (evidence for the exclusion of the surface OH vibration mode), assigned to an electronic transition from an occupied surface electron trap 0.42 eV below the conduction band. The deep trapped electron has also been evidenced by the absorption of surface Ti(III)-OH at 3716 cm^{-1}. In general, the broad IR absorption with a λ^p intensity/wavelength dependence was attributed variously to the absorptions of free electrons and shallow trapped electrons; however it lacks unification about the main contributions to the broad IR absorptions.

Therefore, a detailed mechanism of surface traps and interparticle electron transport in the TiO_2 nanocrystalline film and nanoparticles has yet to be established. To achieve this goal, it is essential to prepare an appropriate TiO_2 film sample that can prevent the interconnection of TiO_2 nanoparticles and avoid the surface contamination by active species such as organic molecules, oxygen gas, and water. In the present studies, we have prepared a TiO_2-xSiO_2 core/shell composite film, in which the TiO_2 nanoparticles were embedded inside the SiO_2 matrix. In principle, interconnection between TiO_2 nanoparticles can be prevented during the sintering of the film, and the surface adsorbates can be reduced substantially after firing at elevated temperature. By the time-resolved spectroscopic studies of TiO_2 nanocrystalline and TiO_2-xSiO_2 core/shell films in the visible (400 to 710 nm) and mid-IR (5.0 to 6.5 μm) ranges, their photoinduced visible and mid-IR transient absorption spectra, together with the corresponding carrier relaxation kinetics, are compared. Three typical carrier relaxation processes on the TiO_2 film have been identified unambiguously, that is, carrier recombination within the lattice, deep trap filling, and interparticle electron transport together with deep trapped electron recombination.

2. Experimental Section

2.1. Sample Preparation. TiO_2 anatase nanoparticles (6 nm) were prepared by the reported hydrolysis method;[27] that is, 0.55 mL of nitric acid (w/w: 65−68%) was dropped in 150 mL of distilled water below 0 °C in a salt−ice bath, and then a solution of 25 mL of $Ti(OCH(CH_3)_2)_4$ mixed with 10 mL of 2-propanol was added to the cooled water in drops for a period longer than 1 h, while keeping the solution stirred vigorously. The mixture was stirred for another 12 h at a temperature of 80 °C. The resulting TiO_2 colloidal solution was vaporized by a rotary evaporator below 40 °C, giving rise to powdered TiO_2 nanoparticles.

TiO_2-xSiO_2 core/shell composites were synthesized by chemical deposition of as-prepared TiO_2 nanoparticles with amorphous SiO_2 in aqueous solution. Briefly, 2.5 g of TiO_2 powder was dispersed in 25 mL of distilled water, and then 0.07 mL of 0.08 M $(NaPO_3)_6$ was dropped into the TiO_2 colloidal solution, keeping ultrasonification for 15 min. Under vigorous stirring, the pH of this mixture was adjusted to 9.5 by adding an appropriate amount of 0.5 M NaOH solution; then a known amount of a 0.5 M Na_2SiO_3 solution was added dropwise to the mixture, the pH was controlled to 9.5 by adding 1% H_2SO_4, and the mixture was aged at 90 °C in a temperature-controlled oil bath for 1 h. Finally, the mixture was separated by centrifugation and the precipitate was washed thoroughly with distilled water and then dried at 105 °C in air for 24 h.

The film samples were prepared by the doctor-blading method.[28] Briefly, TiO_2 or TiO_2-xSiO_2 core/shell colloid solution was added with a small amount of acetylacetone and detergent (Triton X-100) was spread on a CaF_2 plate substrate with a glass rod. The thickness of film was 4−5 μm. After the sample was air-dried, the plate was fired for 30 min at 450 °C in air.

Polished rutile crystal of 1 in. in diameter and 1 mm in thickness was obtained commercially (Hefei Kejing Materials Technology Co., Ltd., China).

2.2. TEM Measurements. Transmission electron microscopy (TEM) images were taken on a JEM-2010 electron microscope. The diluted colloid solutions were dropped on a carbon film supported by a Cu grid substrate. The maximum electron penetration depth of TEM is 70−80 nm.

2.3. Time-Resolved IR and Visible Transient Absorbance Difference Spectroscopic Measurements. The 355 nm excitation pulse was generated by a Nd:YAG laser (Spectra Physics Co., Lab 170; repetition rate, 10 Hz; pulse width, 10 ns). The mid-IR probe beam was generated by a liquid-N_2-cooled cw CO laser (made in Dalian University of Technology, China), which was tunable from 5.0 to 6.5 μm with a spectral spacing around 4 cm^{-1}. The 355 nm excitation pulse energy was 3.6 mJ/pulse, and the size of the defocused IR beam was about 3 mm in diameter. A germanium filter was used to adjust the intensity of the mid-IR probe beam. The transmitted IR probe beam was detected by a MCT (Mercury-Cadmium-Telluride)

detector (Kolmar Technology, model KV104-0.5-A-3/8), and its photocurrent output was amplified by a current preamplifier (Kolmar Technology, model KA020-A1) and filtered by a low band-pass filter (20 MHz∼DC). Finally, the signal was acquired by a digital oscilloscope (Tektronix TDS500D) and the data was transferred to a personal computer. The transient response in absorbance as small as 10^{-4} was detected by signal averaging of 100 laser shots.

For visible transient absorbance difference measurements, the pulse energy was 6 mJ/pulse, and the size of the defocused IR beam was about 1 cm in diameter. A 500 W xenon arc lamp was used as the probe light source. The transmitted light was dispersed in a monochromator and detected by a six-stage photomultiplier (R456, Hamamatsu). The output was amplified by voltage amplifier (SR440, 300 Hz to DC, Stanford Research Systems, Inc). The data acquisition system was the same as that used in the IR detection.

3. Results and Discussion

3.1. TEM Image of TiO_2 and TiO_2-xSiO_2 Core/Shell Nanoparticles. Owing to its anomalously high stability, chemical inertness, and optical transparency, SiO_2 has been used widely as a coating material for core/shell structured nanoparticles.[29,30] The advantages of a core/shell structure are that its stability and chemical activity are determined mainly by the shell material. Therefore, the property of TiO_2-xSiO_2 core/shell structure would be determined by the SiO_2 matrix. Using SiO_2 as an encapsulating shell of TiO_2 would prevent the interconnection of TiO_2 nanoparticles. Figure 1a and b shows the TEM image of TiO_2 nanoparticles and TiO_2-xSiO_2 core/shell nanoparticles, respectively. It is noted that those nanosized TiO_2 particles with diameters around 6 nm are embedded inside the SiO_2 matrix in the core−shell composites. The TiO_2 has a crystal structure revealed by the crystal lattice, and the SiO_2 matrix has an amorphous phase that exhibits as amorphous layer surrounding the TiO_2 nanocrystal. The d value of the TiO_2 lattices is about 3.51 Å, which corresponds to that of anatase (001).[31] Though the carbon substrate is also amorphous, its TEM image exhibits as a light background and can be easily distinguished from that of the SiO_2 matrix.

3.2. Comparison of the Photoinduced Transient Absorption Spectra of Rutile TiO_2 Crystal, Anatase TiO_2 Nanocrystalline, and TiO_2-xSiO_2 Films. Figure 2 shows the photoinduced transient mid-IR absorption spectrum of rutile TiO_2 crystal, anatase TiO_2 nanocrystalline, and TiO_2-xSiO_2 core/shell films, respectively. The observed spectra are featureless in the infrared spectral region, consistent with the carrier IR absorption spectra reported by the other groups.[22−26] The broad, featureless IR signal is assigned to the free conduction-band electrons according to the spectral line shape. This results in an increasing absorption of radiation with increasing wavelength.[27] The absorbance profiles can be described by the following intensity/wavelength relationship[32]

$$c = A\lambda^p \tag{1}$$

where c is the absorption coefficient, λ is the wavelength, p is the scattering constant, and A is a constant. The absorption reaches a broad maximum at what is described as a plasma frequency. According to the semiconductor theory, the value of p depends on the interaction of the plasmon with acoustic phonons, optical phonons, or ionized impurities. For the free carrier intraband transition, absorption of a photon is associated with scattering of phonons or ionized impurities, and the value of p depends on the scattering mechanism. In an ideal case, p assumes a value of $^3/_2$, $^5/_2$, and $^7/_2$ for scattering of acoustic phonons, optical phonons, and ionized impurities, respectively.[33] Dipole oscillations in polar semiconductors (e.g., TiO_2) result

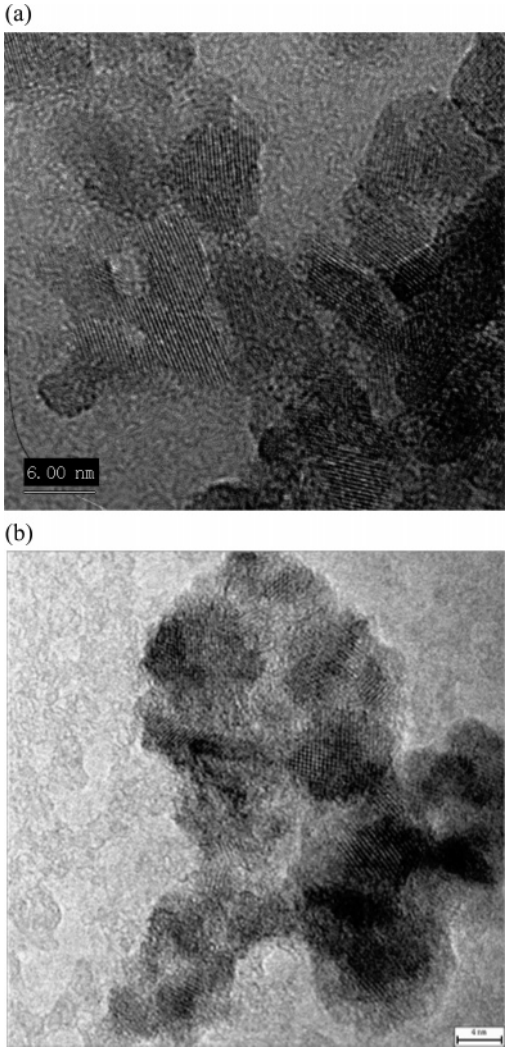

Figure 1. High-resolution TEM image of (a) 6 nm TiO_2 nanoparticles and (b) 6 nm TiO_2-xSiO_2 core/shell nanoparticles.

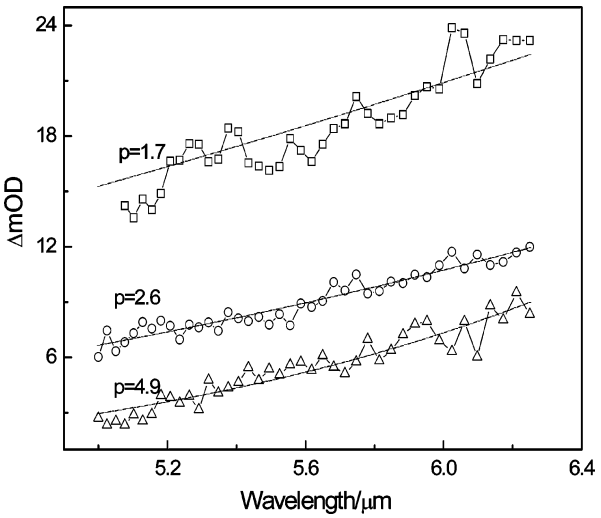

Figure 2. Transient absorption spectrum of TiO_2 rutile crystal (□), TiO_2 film (○), and TiO_2-xSiO_2 core/shell film (△) in the mid-IR range, delayed at 0.2 μs after 355 nm excitation. The dashed line represents the theoretical curve λ^p. All in N_2 saturated ambience.

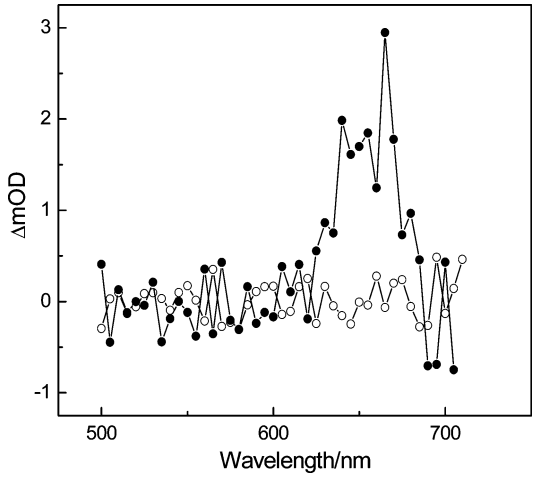

Figure 3. Transient absorption spectrum of TiO_2 film (●) and TiO_2-xSiO_2 core/shell film (○) in the visible range, delayed at 5 μs after 355 nm excitation. Both in N_2 saturated ambience.

in both longitudinal and transverse phonons. Because of the longitudinal nature of the plasmon, it can strongly couple with the longitudinal optical phonons.[34] Free conduction-band electrons are tightly coupled with lattice phonons (acoustic) to conserve momentum during intraband transitions. The electron carriers resulting from the lattice defects are responsible for a plasmon mode that couples with the longitudinal-optical phonon modes. Fitting the experimental data into above relation, p was determined as 1.7, 2.6, and 4.9 for rutile TiO_2 crystal, anatase TiO_2 nanocrystalline, and TiO_2-xSiO_2 core/shell films, respectively. For the rutile TiO_2 crystal, it has an ideal lattice structure and low surface trap density; the experimentally determined p is in agreement with that of the other groups,[35] revealing that the free carrier absorption in the rutile TiO_2 crystal is mainly by the acoustic phonon scattering mechanism. Instead, the TiO_2 nanocrystalline film has a large amount of surface trap states during the preparation process;[36] the value of p is close to that for optical phonon scattering. For the TiO_2-xSiO_2 core/shell film, the value of p obviously deviates from that of the phonon scattering mechanism and is closer to that of impurity ionization scattering.

Figure 3 presents the photoinduced transient absorption spectrum of the TiO_2 nanocrystalline film and the TiO_2-xSiO_2 core/shell film, respectively, in the visible region. In Figure 3, a transient absorption peak located at about 650 nm was observed only for the TiO_2 nanocrystalline film, which can be assigned as the trapped electron absorption based on the reported absorption spectra of the trapped electrons observed for TiO_2.[37−40] It has been shown that a broad visible band with a maximum at 620 nm was assigned to the trapped electron absorption in acid solutions, while an absorption band around 780 nm was assigned to the trapped electron in the alkaline solutions.[41] Bahnemann et al.[38] obtained the absorption spectrum of trapped electrons localized at 650 nm in the presence of a hole scavenger in the visible range. The electron pulse radiolysis technique is another method of obtaining the electron absorption spectrum in TiO_2 nanoparticles, and this technique allows the production of electrons only deposited in nanoparticles.[42] Because in the radiolysis method excess electrons can be deposited easily on the TiO_2 nanoparticles, while the deep traps have been filled, this infers that the 650 nm absorption can arise from the conduction-band or shallow trapped electrons. For photoinduced carriers in the TiO_2 nanocrystalline film, electrons and holes are generated in pairs. It is generally accepted that holes are trapped by surface-bonded hydroxyl groups in the absence of extra hole scavengers.[43−45] Bahnemann et al.[43] have reported that the valence-band holes trapped by the surface hydroxyl groups of colloidal TiO_2 has a maximum absorption around 450 nm. We have tried to detect the trapped hole absorption in the expected spectral region; however, our efforts failed. This is probably because our detection limit of the instrument may not be sensitive enough to probe the hole absorption. In contrast, within our detection limit, no surface-trapped electron absorption at 650 nm can be found for the TiO_2-xSiO_2 core/shell film. Therefore, this fact indicates that the passivation of the TiO_2 nanocrystal with the SiO_2 encapsulating shell has effectively reduced the density of surface-trapped states, providing a direct evidence that the 650 nm absorption arises from the photoinduced shallow trapped electrons. In the TiO_2 crystal, each Ti atom is octahedrally coordinated to the oxygen atoms. At the surface, because of the truncation of the crystal lattice, the coordination numbers of the surface Ti atoms are unsaturated, creating an oxygen vacancy and Ti^{3+} trap states. When SiO_2 is deposited on the TiO_2 surface, Ti−O−Si bonds would be formed on the interface between TiO_2 and SiO_2 phases, which substantially reduces the amount of coordination unsaturated surface Ti atoms, hence the surface trap states.[44] Embedding of the anastase TiO_2 particles into the SiO_2 matrix through Si−O−Ti bonds in the interface would lead to a difference in the band gap between the TiO_2-xSiO_2 core/shell, that is, TiO_2(anatase) has a band gap of ca.3.3 eV, whereas the band gap for titania−silica can be increased up to 4.1 eV.[46] The increase in the band gap also creates an energy barrier to effectively prevent the photogenerated electron within the TiO_2 phase from migrating into the SiO_2 phase, which would hinder the interparticle electron transport for the TiO_2-xSiO_2 core/shell film.

3.3. Comparison between Carrier Relaxation Dynamics of TiO_2 Nanocrystalline and TiO_2-xSiO_2 Core/Shell Films in the Visible and Mid-IR Ranges. Carrier relaxation kinetics have been investigated in both the IR and the visible regions; however, comparisons of the relaxation kinetics in both spectral regions have scarcely been reported. McClendon and Bowman and co-workers[45,47] have studied electron trapping in 2 nm TiO_2 and CdS nanoclusters in the visible range and proposed a kinetically distinct mechanism involving slower electron transport via surface trap-to-trap hopping. They proposed that the electron becomes trapped quickly in a shallow trap at the surface after excitation. Once trapped, thermal fluctuations allow the electron to move from trap site to trap site via the conduction band and/or by direct trap-to-trap hopping. The electron migrates in this way until a deep trap is encountered from which it cannot escape. Because thermal fluctuations can drive the shallow trapped electron into the conduction band, it is expected that shallow trapped electrons would behave like free carriers once they are thermally excited into the conduction band.

Figure 4 gives the typical temporal profiles of the transient absorption of a 6 nm TiO_2 crystalline film (Figure 4a−d), a 6 nm TiO_2-xSiO_2 core/shell film (Figure 4e−h), and a 10 nm SiO_2 film (Figure 4h) observed at 1800 cm^{-1}. Kinetics detected at other wavelengths are very similar. In Figure 4, three typical kinetic phases can be observed for the TiO_2 nanocrystalline film. The first phase begins at 0 up to 300 ns after laser excitation (Figure 4a); a rapid decay beyond the detection limit of the instrumental response (80 ns) shows the carrier recombination kinetics occurring in the bulk TiO_2 nanocrystal. The second starts from 0.5 μs up to about 4 μs (Figure 4b), in which a small-amplitude bleaching recovery can be identified. Though the bleaching recovery signal is weak, its kinetic feature has

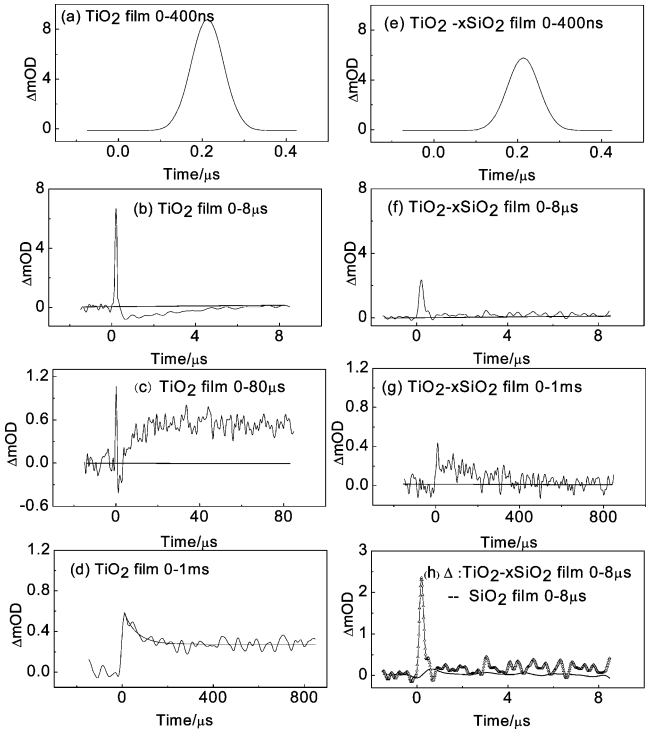

Figure 4. Temporal profiles of transient absorption probed at 1800 cm^{-1} after excitation at different time domains: (a) 0−400 ns, (b) 0−8 μs, (c) 0−80 μs, and (d) 0−1 ms for TiO_2 film and (e) 0−400 ns, (f) 0−8 μs, and (g) 0−1 ms for TiO_2-xSiO_2 core/shell film; (h) 0−8 μs for TiO_2-xSiO_2 film (△) and SiO_2 film (dashed lines) in comparison. All in N_2 saturated ambience.

been confirmed with confidence by repeated experiments. This phenomenon can be interpreted in terms of deep trap states filled by the shallow trapped carriers. A femtosecond time-resolved IR difference absorbance study of photoinduced charge recombination in a dye-sensitized TiO_2 nanocrystalline film shows that the injected electrons within the conduction band would relax in its energy and the injected electrons would finally relax from the shallow trap states to the deep trap states.[21,48] The energy relaxation rate is believed to be dependent on the densities of the trap states, which decrease exponentially with the increasing trap depth relative to the conduction band.[48] Szczepankiewicz et al. reported a surface-trapped state that locates 0.42 eV below the conduction band in a TiO_2 polycrystalline sample (Degussa P-25).[22] Other groups such as Hagfeldt's and McQuillan's have reported IR absorptions from the shallow trapped electrons located 0.1−0.25 eV (about 800−2020 cm^{-1}) below the conduction band.[34,49] Onishi and co-workers assumed that electrons in the conduction band and shallow traps have constant absorption in the mid-IR range and the electrons would have a zero absorption once they decay to deep traps.[50] With this assumption, for a nanoparticle with shallow trapped electrons, the shallow trapped electrons would contribute to the IR absorption in the detected spectral region (1800 cm^{-1}) prior to the band gap excitation. This absorption is caused by the electron transition from the shallow trap sites to the bottom of the conduction band. Because the band gap of TiO_2 is 3.2 eV, when excited at 355 nm (3.48 eV) hot photogenerated electrons locating 0.28 eV above the bottom of the conduction band are thus produced. These hot electrons would relax to the bottom of the conduction band. Once the empty energy levels near the bottom of the conduction band are occupied, transitions from the shallow trap sites to the conduction band are suppressed, which gives rise to a bleaching signal in the probed wavelength accordingly. When the photogenerated electrons at the bottom

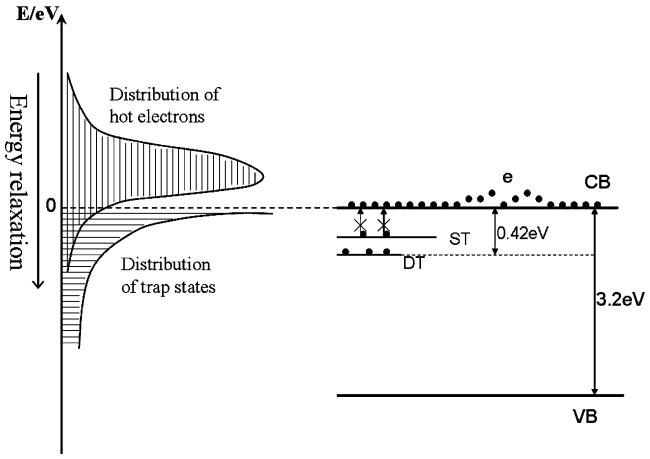

Figure 5. Schematic illustrations for the photogenerated hot electrons relaxing into the trap states, where DT and ST represent deep traps and shallow traps, respectively.

of the conduction band relax further down to the trap sites, the occupancy of the energy levels near the bottom of the conduction band become cleared gradually and the absorption of the shallow trapped electrons would be restored. This process corresponds to the bleaching recovery phase of the observed kinetics. When all of the photogenerated electrons relax into the trap sites, enhanced IR absorption occurs as observed in the absorption rising and decay phases. Figure 5 presents a schematic diagram for the hot electron relaxation. The ratio of the maximum recovered absorption over that of the bleaching (3:1) roughly reflects the population ratio of the photogenerated trapped electrons and the trapped electrons as-prepared in the TiO_2 nanoparticles. A detailed model is proposed as follows.

A Gaussian-type of energy distribution for the hot photogenerated electrons within the conduction band $\rho(E^*) = (1)/(\sigma\sqrt{2\pi}) \exp[(-(E^* - E_0)^2)/(2\sigma^2)]$ is assumed as shown in Figure 5, where E^* denotes the energy, $\rho_c(E^*)$ is the population density of the hot electrons, σ is the fwhm (full width at half-maximum) of the Gaussian function, and E_0 is the peak position. These electrons would finally fill into the shallow trap states described by an exponential type of density-of-states function

$$\rho_T(E) = \alpha \exp(-\alpha E) \tag{2}$$

where E is the trapping energy relative to the bottom of the conduction band at which E is set to zero. We further assume that the energy relaxation occurs mainly within the neighboring states and the relaxation rate is proportional to the density of the states,[51] that is

$$\frac{dE}{dt} = \beta \rho_T(E) \tag{3}$$

where $\rho_T(E)$ indicates the function of the density-of-states for the trap states and β is a constant. Combining eqs 2 and 3, together with a initial condition that $E = 0$ at $t = 0$, we obtain

$$E(t) = \frac{\ln(\alpha^2 \beta t + 1)}{\alpha} \tag{4}$$

Because $\rho_T(E)$ is an exponential function that leads to the relaxation of the hot electrons in an unsymmetrical way, that is, the lower-energy half of the hot electrons defined by the Gaussian function relaxes faster than its higher-energy counterpart.

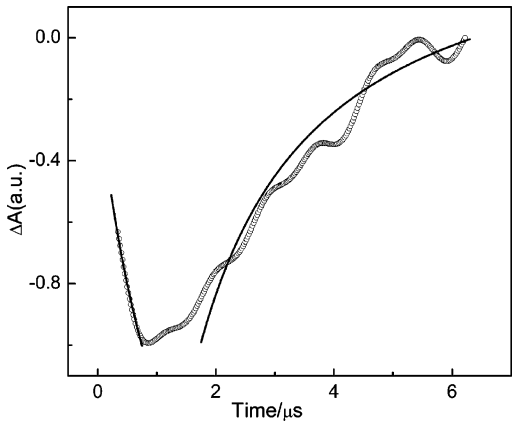

Figure 6. Fitting of the bleaching and bleaching recovery of a 6 nm TiO_2 film after 355 nm laser excitation by the theoretical model. Open circles, experimental data; solid lines, fitting curves. Bleaching phase is fitted by eq 8, and bleaching recovery, by eq 9. Fitting parameters: $\alpha^2\beta = 2.86\ \mu s^{-1}$, $\gamma = 2.1\ eV^{-1}$.

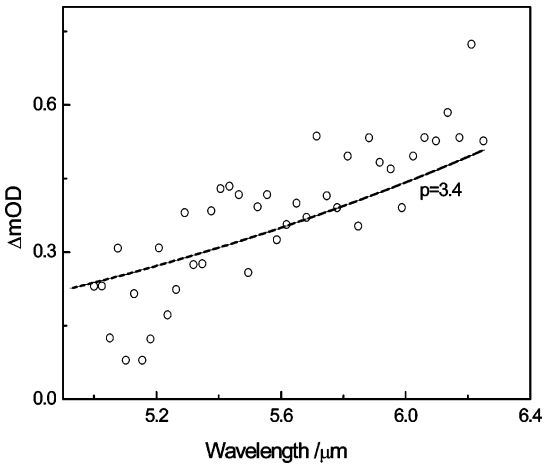

Figure 7. Transient absorption spectrum of TiO_2 nanocrystalline film (○) delayed at 50 μs after 355 nm excitation. The dashed line represents the fitting curve of $c = A\lambda^p$.

For simplicity, the Gaussian type of distribution function is approximated by two branches of exponential functions with peaks at $E_0^* = 0$, that is

$$\rho_c(E^*) = \exp \gamma E^* \quad -\infty < E^* \le 0 \tag{5}$$

$$\rho_c(E^*) = \exp(-\gamma E^*) \quad 0 \le E^* < +\infty \tag{6}$$

where γ is a fitting parameter. By applying the population conservation constraint, that is, the population lost in the hot electron equals that gained in the trap states, we can write the following equation for the lower-energy branch

$$\int_{-\infty}^{E^*} \rho_c(E^*)dE^* = \int_0^E \rho_T(E)dE \quad E^* \le 0 \tag{7}$$

Combining eqs 2, 4, and 5, we have

$$E^*(t) = \frac{1}{\gamma}\ln\left(\gamma - \frac{\gamma}{\alpha^2\beta t + 1}\right)$$

And the population for the hot electrons of the lower-energy branch at the bottom of the conduction band at a given time t is

$$\rho_L(t) = \gamma - \frac{\gamma}{\alpha^2\beta t + 1}, \quad 0 \le t \le \frac{1}{\alpha^2\beta(\gamma - 1)} \tag{8}$$

In a similar way, the population for the hot electrons of the higher-energy branch at the bottom of the conduction band at a given time t can be derived as

$$\rho_H(t) = 2 - \gamma + \frac{\gamma}{\alpha^2\beta t + 1}, \quad t \ge \frac{1}{\alpha^2\beta(\gamma - 1)} \tag{9}$$

where the subscripts "L" and "H" of $\rho(t)$ stand for the lower- and higher-energy branches of the hot electrons, respectively. Obviously, the magnitude of the bleaching signal ($-\Delta A$) would be proportional to the population of the hot electrons on the bottom of the conduction band. Therefore, eqs 8 and 9 can be used to describe the bleaching and bleaching recovery phases, respectively. Figure 6 presents the fitting of the bleaching and bleaching recovery kinetics; the model does describe a faster bleaching and a slower bleaching recovery. It should be noted that the bleaching signal may also be contributed from the stimulated emission, which remains to be verified. Our model clearly reveals that the bleaching recovery phase comes from the filling of deep trap states by the shallow trapped electrons.

The third phase is a very slow decay absorption corresponding to the carrier recombination. As discussed above, at this stage the deep trapped levels have been filled by the shallow trapped electrons and the remaining shallow trapped electrons can be thermally excited into the conduction band, giving rise to the IR absorption. Because the electrons are trapped mainly at the surface, it is expected that their IR absorption spectrum could be different from that of the free carrier within the lattice. Figure 7 presents the shallow trapped absorption at a delay time of 50 μs. At this delay time, the IR absorption is mainly from the thermally activated trapped electrons. Fitting the spectrum into relation 1, the scattering constant obtained equals 3.4, instead of 2.6 for the free carriers in the lattice observed for the TiO_2 nanocrystalline film. This value of p is close to that for scattering by the impurities, which is in agreement with the fact that electrons are trapped at the surface where more defects and impurities are present than in the lattice. Therefore, the corresponding slow kinetic phase is assigned to the carrier recombination of the shallow trapped electrons. The population of the trapped electrons on the different trap levels follows the Boltzmann equation, and the trapped electrons are mobile according to a mechanism of trapping/detrapping through the conduction band by thermal activation.[52] Boschloo[53] and more recently Hagfeldt[49] also reported that the release of immobile electrons from occupied traps to the conduction band is a thermally activated process in a multiple-trapping model, and the apparent electron diffusion coefficient should depend strongly on temperature. The thermally activated detrapping rate is given by $k_d(\epsilon) = \nu_0 \exp(-\epsilon)$, where ν_0 is the attempt-to-escape frequency, ϵ is the trap energy in units of k_BT, and that of the conduction band is set to zero. An estimation of ν_0 is that it should not exceed the vibration frequency of titanium atoms within the lattice, that is, $\nu_0 \sim 4 \times 10^{12}\ s^{-1}$.[54] This relation implies that the deeper the electron is trapped the slower it would be detrapped. Giving a typical trapping energy of 0.42 eV, the estimated detrapping time constant is about 20 μs. Considering the interparticle electron transport process, the carrier recombination process can be very slow. This has been confirmed experimentally by Durrant et al.[11−13] and interpreted by a number of theoretical models such as continuous-time random walk (CTRW)[55−58] and the random flight models.[51,52] When compared to the relaxation kinetics of the TiO_2 film, only the first rapid decay process can be observed for the TiO_2-xSiO_2

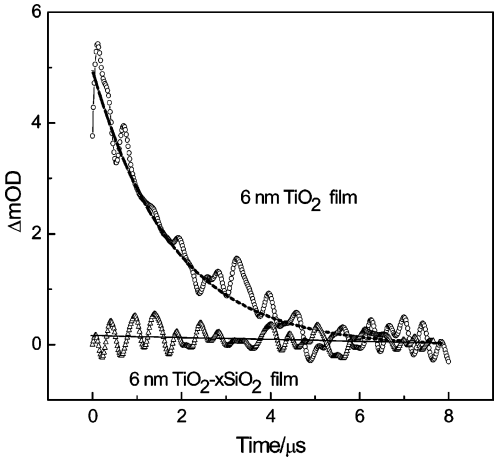

Figure 8. Time profiles of transient absorption of TiO_2 film (○) and TiO_2-xSiO_2 core/shell film (△) observed at 650 nm, both in N_2 saturated ambience. The profile can be fitted by monoexponential decay; the dashed lines represent the fitting profile.

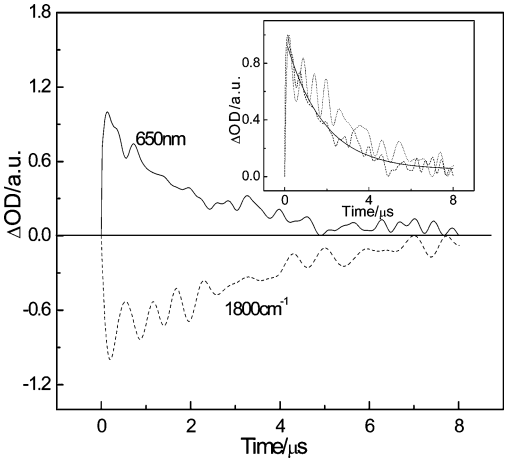

Figure 9. Comparison of the bleaching recovery phase of the trap filling process detected in the mid-IR region and the decay profile of the shallow trapped electron absorption observed at 650 nm. Both of the two temporal profiles are normalized. The inset shows the overlap of the inverted bleaching recovery kinetic trace with the decay trace probed at 650 nm. The solid line is the fitting of the monoexponential decay.

core/shell film, that is, the fast rising and decay beyond the instrumental detection limit in the temporal window from 0 up to 300 ns (Figure 4e), which is similar to its counterpart in the TiO_2 nanocrystalline film. This indicates that the passivation of the TiO_2 nanoparticle with the SiO_2 shell in the TiO_2-xSiO_2 core/shell structure would not affect the free carrier recombination kinetics within the crystal lattice, though the scattering mechanism for the intraband transition of the carriers is obviously different. Interestingly, the follow-up bleaching recovery phase and the slow decay phase cannot be observed within the limit of the instrumental resolution. The fact again gives strong support to the fact that the passivation of the TiO_2 nanocrystal with the SiO_2 matrix "heals" the surface trap states as well as prevents interparticle electron transport. Accordingly, the slow kinetic phase observed in the TiO_2 nanocrystalline film is assigned to the interparticle electron transport and deep trapped electron recombination.

To further examine the trapped electron−hole recombination dynamics, we measured the decay profile of the transient absorption at 650 nm of the shallow trapped electrons. Figure 8 shows the relaxation kinetics of the surface-trapped electrons detected at 650 nm for the TiO_2 nanocrystalline film, and the corresponding temporal profile of transient absorption for the TiO_2-xSiO_2 core/shell film, which acts as a baseline, is also presented for comparison. For the TiO_2 nanocrystalline film, the decay curve for the trapped electrons can be fitted by a single-exponential decay with a time constant of about 1.8 μs. As we discussed above, the filling process of the deep trapped sites by the free carriers detected by IR absorption has a bleaching recovery process. To interpret the relationship between the bleach recovery process and the relaxation of shallow trapped electrons, Figure 9 presents a further comparison between the rising phase of the deep trap filling (Figure 4c) and the visible absorption decay profile of the trapped electron for the TiO_2 film (Figure 8). Figure 9 reveals that the trapped electron relaxation kinetics observed at 650 nm in the visible region coincides with the deep trap filling process observed in the mid-IR region. This fact supports the assignment that the carrier absorption at 650 nm arises from the shallow trapped electrons, whereas the relaxation kinetics with a time constant of about 1.8 μs arises from the deep trap filling process. It should be noted that in the visible decay profile we did not observe the electron transport process at a longer time scale, and this is possibly due to the instrumental limitation of sensitivity.

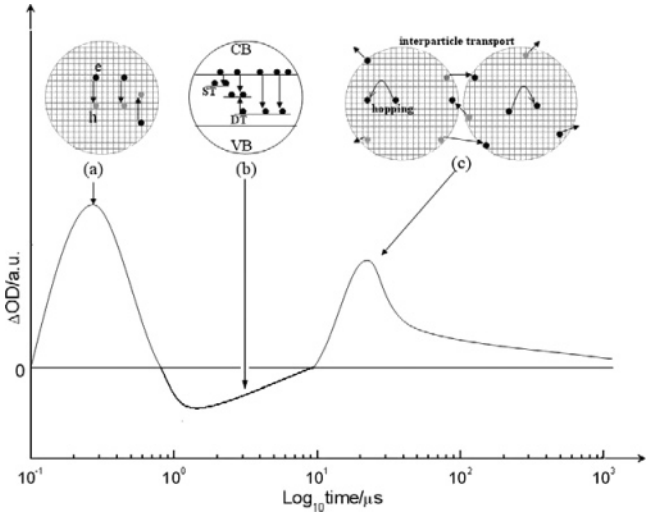

Figure 10. Schematic illustration of the three typical charge recombination processes occurring at TiO_2 nanocrystalline film: (a) free carrier recombination in the TiO_2 crystal lattice; (b) trap filling by the shallow trapped carriers, where DT and ST represent deep traps and shallow traps, respectively; (c) interparticle electron transport and deep trapped electron recombination.

In summary, our comparative study of photoinduced carrier absorption spectra and the corresponding kinetics for TiO_2 nanocrystalline film and TiO_2-xSiO_2 core/shell film in both the visible and mid-IR spectral regions gives a consistent result regarding the carrier relaxation process. The three typical relaxation phases and their physical nature are illustrated schematically in Figure 10.

4. Conclusions

We have investigated TiO_2 nanocrystal and TiO_2-xSiO_2 core/shell films by detection of the photoinduced carriers with time-resolved transient absorption spectroscopy in both the visible and the mid-IR range. By analysis of the photoinduced carrier absorption spectra and the corresponding relaxation kinetics, we come to the following conclusions:

(1) Conduction-band electrons within the lattice and the shallow trapped electrons at the surface of the TiO_2 nanocrys-

talline film can be distinguished by their IR absorption spectra rationalized in an intensity−wavelength relation, that is, $c = A\lambda^p$. For the conduction-band electron p is determined as 2.6, whereas for the shallow trapped electrons p is 3.4 for 6 nm nanocrystals.

(2) The shallow trapped electron has a visible absorption peak around 650 nm, and its relaxation kinetics with a time constant of about 1.8 μs corresponds to the deep trap sites filling.

(3) The photoinduced carrier relaxation for the TiO_2 nanocrystalline film consists of three typical kinetic phases, that is, a rapid decay for conduction-band electrons within the lattice with an upper decay time limit of 80 ns restricted by the instrumental response time, a deep trap level filling process with a time constant of about 1.8 μs, and a very slow decay kinetic process corresponding to the interparticulate carrier transport and deep trapped electron recombination.

(4) Passivation of the TiO_2 nanocrystalline with the SiO_2 shell reduces the density of the trapped state on the TiO_2 nanoparticle surface substantially and blocks the interparticle carrier migration effectively.

Acknowledgment. We thank Prof. Y. Lin. (Institute of Chemistry, Chinese Academy of Sciences) for help in the preparation of the TiO_2 film, and Prof. C. R. Li and Mr. X. A. Yang (Institute of Physics, Chinese Academy of Sciences) for their help in taking the TEM images for the TiO_2 and $TiO_2-x SiO_2$ core/shell nanoparticles. This research was supported by CAS innovative project (KJCX-H2-03), NSFC under grant nos. 60321003 and 60438020.

References and Notes

(1) Kraeulter, B.; Bard, A. J. *J. Am. Chem. Soc.* **1978**, *100*, 2239.
(2) Fujihira, M.; Satoh, Y.; Osa, T. *Nature* **1981**, *293*, 206.
(3) Matthews, R. W. *J. Phys. Chem.* **1987**, *91*, 3328.
(4) Turchi, C. S.; Ollis, D. F. *J. Catal.* **1990**, *122*, 178.
(5) Fujishima, A.; Rao, T. N.; Tryk D. A. *J. Photochem. Photobiol. C* **2000**, *1*, 1.
(6) Fujishima, A.; Hashimoto, K.; Watanabe, T. *Photocatalysis*; BKC Inc: Tokyo, 1999.
(7) O'Regan, B.; Grätzel, M. *Nature* **1991**, *353*, 737.
(8) Nazeeruddin, M. K.; Kay, A.; Rodicio, I.; Humphry-Baker, R.; Muller, E.; Liska, P.; Vlachopoulos, N.; Grätzel, M. *J. Am. Chem. Soc.* **1993**, *115*, 6382.
(9) Hoffmann, M. R.; Martin, S. T.; Choi, W.; Bahnemann, D. W. *Chem. Rev.* **1995**, *95*, 69.
(10) Szczepankiewicz, S. H.; Moss, J. A.; Hoffmann, M. R. *J. Phys. Chem. B* **2000**, *104*, 9842.
(11) Haque, S. A.; Tachibana, Y.; Klug, D. R.; Durrant, J. R. *J. Phys. Chem. B* **1998**, *102*, 1745.
(12) Haque, S. A.; Tachibana, Y.; Willis, R. L.; Moser, J. E.; Grätzel, M.; Klug, D. R.; Durrant, J. R. *J. Phys. Chem. B* **2000**, *104*, 538.
(13) Tachibana, Y.; Haque, S. A.; Mercer, I. P.; Durrant, J. R.; Klug, D. R. *J. Phys. Chem. B* **2000**, *104*, 1198.
(14) Hagfeldt, A.; Grätzel, M. *Chem. Rev.* **1995**, *95*, 49.
(15) Redmond, G.; Fitzmaurice, D.; Grätzel, M. *J. Phys. Chem.* **1993**, *97*, 6951.
(16) Rothenberger, G.; Moser, J. M.; Grätzel, M.; Serpone, N.; Sharma, D. K. *J. Am. Chem. Soc.* **1985**, *107*, 8054.
(17) Kay, A.; Humphrey-Baker, R.; Grätzel, M. *J. Phys. Chem.* **1994**, *98*, 952.
(18) Howe, R. F.; Grätezl, M. *J. Phys. Chem.* **1985**, *89*, 4495.
(19) Linsebigler, A. L.; Lu, G.; Yates, J. T. *Chem. Rev.* **1995**, *95*, 735.
(20) Berger, T.; Sterrer, M.; Diwald, O.; Knözinger, E.; Panayatov, D.; Thompson, T. L.; Yates, J. T., Jr. *J. Phys. Chem. B* **2005**, *109*, 6061.
(21) Ghosh, H. N.; Asbury, J. B.; Weng, Y. X.; Lian, T. *J. Phys. Chem. B* **1998**, *102*, 10208.
(22) Szczepankiewicz, S. H.; Moss, J. A.; Hoffmann, M. R. *J. Phys. Chem. B* **2002**, *106*, 2922.
(23) Yamakata, A.; Ishibashi, T.; Onishi, H. *J. Phys. Chem. B* **2001**, *105*, 7258.
(24) Yoshihara, T.; Katoh, R.; Furube, A.; Tamaki, Y.; Murai, M.; Hara, K.; Murata, S.; Arakawa, H.; Tachiya, M. *J. Phys. Chem. B* **2004**, *108*, 3817.
(25) Yamakata, A.; Ishibashi, T.; Onishi, H. *J. Phys. Chem. B* **2001**, *333*, 271.
(26) Szczepankiewicz, S. H.; Moss, J. A.; Hoffmann, M. R. *J. Phys. Chem. B* **2002**, *106*, 7654.
(27) O'Regan, B.; Moser, J.; Anderson, M.; Grätzel, M. *J. Phys. Chem.* **1990**, *94*, 8720.
(28) Nazeeruddin, M. K.; Kay, A.; Rodicio, I.; Humphry-Baker, R.; Müller, E.; Liska, P.; Vlachopoulos, N.; Grätzel, M. *J. Am. Chem. Soc.* **1993**, *115*, 6382.
(29) Philipse, A. P.; Nechifor, A. M.; Pathmamanoharan, C. *Langmuir* **1994**, *10*, 4451.
(30) Liz-Marzan, L. M.; Mulvaney, P. *J. Phys. Chem. B* **2003**, *107*, 7312.
(31) Burdett, J. K.; Hughbands, T.; Gordon, J. M.; Richardson, J. W., Jr.; Smith, J. V. *J. Am. Chem. Soc.* **1987**, *109*, 3639.
(32) Perkowitz, S. *Optical Characterization of Semiconductors*; Academic Press: London, 1993.
(33) Smith, R. A. *Semiconductors*; Cambridge University Press: Cambridge, U.K., 1978.
(34) Warren, D. S.; McQuillan, J. *J. Phys. Chem. B* **2004**, *108*, 19373.
(35) Baumard, J.-F.; Gervais, F. *Phys. Rev. B* **1977**, *15*, 2316.
(36) Boschloo, G.; Fitzmaurice, D. *J. Phys. Chem. B* **1999**, *103*, 2228.
(37) Martin, S. T.; Herrmann, H.; Choi, W.; Hoffmann, M. R. *J. Chem. Soc. Faraday Trans.* **1994**, *90*, 3323.
(38) Bahnemann, D. W.; Henglein, A.; Lilie, J.; Spanhel, L. *J. Phys. Chem.* **1984**, *88*, 709.
(39) Jalob, M.; Levanon, H.; Kamat, P. V. *Nano. Lett.* **2003**, *3*, 353.
(40) Kölle, U.; Moser, J.; Grätzel, M. *Inorg. Chem.* **1985**, *24*, 2253.
(41) Gao, R.; Safrany, A.; Rabani, J. *Radiat. Phys. Chem.* **2002**, *65*, 599.
(42) O'regan, B.; Grätzel, M.; Fitzmaurice, D. *Chem. Phys. Lett*. **1991**, *183*, 89.
(43) Bahnemann, D. W.; Henglein, A.; Spanhel, L. *Faraday Discuss Chem. Soc.* **1984**, *78*, 151.
(44) Thompson, T. L.; Yates, J. T., Jr. *J. Phys. Chem. B* **2005**, *109*, 18230.
(45) O'Neil, M.; Marohn, J.; McLendon, G. *Chem. Phys. Lett*. **1990**, *168*, 208.
(46) Gao, X. T.; Wachs, I. E. *Catal. Today* **1999**, *51*, 233.
(47) Skinner, D. E.; Colombo, D. P.; Cavaleri, J. J.; Bowman, R. M. *J. Phys. Chem.* **1995**, *99*, 7853.
(48) Weng, Y. X.; Wang, Y. Q.; Asbury, J. B.; Ghosh, H. N.; Lian, T. *J. Phys. Chem. B* **2000**, *104*, 93.
(49) Peter, L. M.; Walker, A. B.; Boschloo, G.; Hagfeldt, A. *J. Phys. Chem. B* **2006**, *110*, 13694.
(50) Takeshita, K.; Sasaki, Y.; Kobashi, M.; Tanaka, Y.; Maeda, S.; Yamakata, A.; Ishibashi, T.-a.; Onishi, H. *J. Phys. Chem. B* **2003**, *107*, 4156.
(51) Katoh, R.; Furube, A.; Barzykin, A. V.; Arakawa, H.; Tachiya, M. *Coord. Chem. Rev.* **2004**, *248*, 1195.
(52) Barzykin, A. V.; Tachiya, M. *J. Phys. Chem. B* **2002**, *106*, 4356.
(53) Boschloo, G.; Hagfeldt, A. *J. Phys. Chem. B* **2005**, *109*, 12093.
(54) Zhang, W. F.; He, Y. L.; Zhang, M. S.; Yin, Z.; Chen, Q. *J. Phys. D: Appl. Phys.* **2000**, *33*, 912.
(55) Scher, H.; Montroll, E. W. *Phys. Rev. B* **1975**, *12*, 2455.
(56) Blumen, A.; Zumofen, G.; Klafter, J. *Phys. Rev. B* **1984**, *30*, 5379.
(57) Nelson, J. *Phys. Rev. B* **1999**, *59*, 15374.
(58) Nelson, J.; Chandler, R. E. *Coord. Chem. Rev.* **2004**, *248*, 1181.